

Target/Background Classification Regularized Nonnegative Matrix Factorization for Fluorescence Unmixing

Binjie Qin, *Member, IEEE*, Chen Hu, and Shaosen Huang

Abstract—Nonnegative matrix factorization (NMF) is usually applied to multispectral fluorescence imaging for fluorescence unmixing. Unfortunately, most NMF-based fluorescence unmixing methods fail to take advantage of spatial information in data. Besides, NMF is an inherently ill-posed problem, which gets worse in the sparse acquisition of multispectral data (from a small number of spectral bands) due to its insufficient measurements and severe discontinuities in spectral emissions. To overcome these limitations by exploiting the spatial difference between multiple-target fluorophores and background autofluorescence (AF), we propose improved normalized cut to automatically classify all multispectral pixels into target fluorophores and background AF groups. We then initialize NMF by extracting the endmember spectra of target/background fluorescent components in the two groups, and impose a $L_{1/2}$ -norm partial sparseness constraint on merely the abundances of target fluorophores within hierarchical alternating least squares framework of NMF. Experimental results based on synthetic and *in vivo* fluorescence data show the superiority of the proposed algorithm with respect to other state-of-the-art approaches.

Index Terms—Fluorescence spectra, insufficient measurements, multispectral imaging, nonnegative matrix factorization (NMF), partial sparseness constraint, signal decomposition, spatial information, target/background classification.

I. INTRODUCTION

IN VIVO multispectral fluorescence imaging instrument has been widely used to measure and/or record cellular and subcellular biological processes in the life and medical sciences, such as drug discovery and disease diagnosis [1]. The vast majority of applications of *in vivo* fluorescence imaging are based on epi-illumination planar imaging, where the exciting source and detectors reside on the same side of the tissue and the measurements are acquired in reflectance mode. Given exciting light sources, different fluorophores

labeled with fluorescent dyes can emit fluorescence photons from visible to near-infrared wavelengths to generate multispectral images. The multispectral images involve multispectral pixels represented by vectors, with each component being a measurement corresponding to the specific wavelengths. This fluorescence imaging instrument enables the simultaneous use of multiple fluorophores to detect and localize particular components of complex biomolecular assemblies in the *in vivo* sample. For most fluorophores, emission spectra are distinct, but often overlap and become indistinguishable in the mixed multispectral images. Hence, spectral unmixing (SUM) [2] is necessary in the multispectral fluorescence imaging instrument to decompose the mixed multispectral images \mathbf{D} into a product of pure spectral signatures \mathbf{S} , i.e., endmembers, and corresponding fractional abundance \mathbf{C} , indicating the proportion of each endmember. If the endmember spectra \mathbf{S} are identified [3] in advance, \mathbf{C} can be easily estimated by the use of supervised SUM methods such as least squares method. However, the factory-provided reference endmember spectra used in the supervised SUM are uncertain and always require extensive calibration efforts for the endmember identification [3]. Therefore, the unsupervised SUM has been developed to simultaneously estimate the spectra and abundances without *a priori* knowledge about endmember spectra.

In designing, implementing, and assessing the fluorescence imaging instrument, there are some practical challenges must be overcome, among which the so-called autofluorescence (AF) [1], [4] can be produced by some proteins such as collagens and other biological materials when they are excited by appropriate visible light in *in vivo* fluorescence imaging. Generally, AF originates from all possible background disturbances, which mainly include two kinds of sources [1], [4]: 1) the AF caused by the natural fluorescent molecules in tissue and food and 2) some instrument-based noise, shading, and leakage light from exciting filters. Therefore, AF stems from various sources covering large background areas, and has a dispersive spatial distribution. Furthermore, the AF wavelength ranging from 400 to 700 nm is overlapped with the emission spectra of most fluorophores. Due to these extensive overlaps occurring between the fluorophores and AF in the spatial and spectral distributions, it is difficult to blindly separate multiple fluorophores from AF when the AF is regarded as a constituent component by the current

Manuscript received July 8, 2015; revised November 13, 2015; accepted November 16, 2015. Date of publication January 25, 2016; date of current version March 8, 2016. This work was supported in part by the National Natural Science Foundation of China under Grant 61271320 and Grant 60872102 and in part by the China Scholarship Council through the Small Animal Imaging Project under Grant 06-545. The Associate Editor coordinating the review process was Dr. Shervin Shirmohammadi.

The authors are with the School of Biomedical Engineering, Shanghai Jiao Tong University, Shanghai 200240, China (e-mail: bj Qin@sjtu.edu.cn).

Color versions of one or more of the figures in this paper are available online at <http://ieeexplore.ieee.org>.

Digital Object Identifier 10.1109/TIM.2016.2516318

unsupervised SUM methods. Alternatively, some hardware-based methods subtract an AF estimate from observation data after using extra excitation filters or extra unlabeled samples to acquire bare AF images [1], [4]. To successfully practice these methods, we must carefully match the specific filter sets with the spectral properties of both AF and fluorophores. In many cases, none of the mentioned methods in the instrument design can fully remove the AF from the fluorescence imaging.

As an unsupervised data decomposition (or blind source separation) technique, nonnegative matrix factorization (NMF) has been successfully applied to blindly separate several source signals in SUM [4], [5], biomedical source separation [6], [7], and nondestructive testing [8]. However, there are three shortcomings. First, NMF suffers from an ill convergence problem such that starting from different initial search [9] points results in different values for the elements of \mathbf{C} and \mathbf{S} matrices. Especially, the ill convergence problem becomes worse when there are insufficient measurements and low spectral resolutions in the sparse acquisition of multispectral fluorescence imaging data from a small number (e.g., 3–10) of spectral bands. However, this sparse acquisition can be fast and cost-effective in clinical applications. Therefore, different NMF studies have proposed appropriate initial values [9] and some additional regularization constraints (such as sparseness [10], [11] and smoothness constraints [8]) to ensure the optimal NMF solution. Second, current sparseness constraints [10], [11] for strengthening part-based representation do not discriminate sparse components from nonsparse components, limiting unmixing accuracy when only some special targets of interest are sparse while a specific background component is nonsparse. In fluorescence imaging, some sparseness-constrained methods [4], [12], [13] update the whole abundance matrix of all components so that the abundance matrices of fluorescent targets and AF may interfere with each other in NMF. Third, NMF does not consider spatial information of neighboring pixels from specific components to find more intuitive and interpretable unmixing solution of abundance matrix \mathbf{C} .

To overcome these limitations of NMF, this paper proposes unsupervised target/background classification regularized NMF (TBCR-NMF)¹ with partial sparseness constraint. The motivation is based on the following two facts. First, multiple fluorophores tend to locally accumulate in specific biological tissues so that their sparse spatial distributions are usually confined to relatively small areas, while background AF propagates at all directions and diffuses widely over large areas. This spatial distribution difference between multiple target fluorophores and background AF is preserved across the whole spectral bands, although the sparse acquisition introduces sharp discontinuity in the spectral emissions across the multiple spectral bands. Second, the set of pixels in the multiple localized fluorophores similarly exhibits high intensities within local patches and can be classified into a single target group, while the set of pixels in the large background areas contains low intensity pixels that can

be grouped as a single background group. This inherent target/background contrast is still preserved across the multiple spectral bands in the fluorescence imaging.

With the above analysis facilitating the development of unsupervised target/background classification without any training samples [2], [14], we propose TBCR-NMF from the following two aspects. First, an unsupervised target/background classification is implemented as a preprocessing that extracts endmembers and corresponding abundances to optimally initialize NMF. In solving the local minimum problem of NMF, most initialization methods [15], [16] have not used the spatial information in the source spectral data and therefore cannot accurately identify the endmembers (and their corresponding abundance) for the near-optimal starting point for NMF. In this paper, initial target/background classification is helpful to discriminably extract the endmembers from the localized target regions and large background regions. Then, we initialize the abundance matrix \mathbf{C} by fixing the spectra \mathbf{S} during the first ten iterations of NMF. Second, the TBCR-NMF facilitates optimal fluorescence unmixing by imposing partial sparseness constraints on the abundances of multiple target fluorophores but not on the abundance of diffusive AF. In summary, classifying mixed multispectral data into two groups is a useful strategy for initializing and regularizing NMF, such that the target/background classification can transfer the classified spatial structures [17] into the accurate and unique solution of NMF-based unmixed results. The most recent trend of utilizing the spatial information and sparsity for unmixing/classification of multispectral image has enabled the realization of some new computing model in multispectral/hyperspectral imaging [18]–[21].

Traditional multispectral image classification [22] methods, such as unsupervised (e.g., K-means, kernel-based nonparametric method) and supervised (e.g., maximum likelihood, support vector machine), have considered the pixel-wise spectral dissimilarity between two pixels to group the image data into a finite number of discrete classes without using spatial dependence. To reduce the labeling uncertainty that exists when only the spectral information is used, recent research has introduced the spatial contextual information into the joint spectral–spatial classification, which generally exploited the highly correlated regional information (entropy, variance, etc.) extracted from the standard (such as the crisp neighbor set employed by Markov random field modeling) or adaptive neighbor system in the image. Rather than defining a crisp neighbor set containing insufficient neighboring samples for every pixel, image segmentation [22] is another approach to include spatial information in classification, enabling the large neighborhood definition by partitioning an image into nonoverlapping large homogeneous regions. Many algorithms have been proposed to address image segmentation problem, such as region-growing algorithms, and watershed methods. In this paper, only binary image segmentation implementing target/background homogeneous region partition is desirable for the subsequent target/background classification.

As an excellent binary image segmentation algorithm, the original normalized cut (Ncut) [23] is done by partitioning all graph nodes (i.e., pixels) of whole image into

¹<http://www.escience.cn/people/bjqin/research.html>

two disjoint parts. Rather than focusing on local features and their neighboring consistencies in the image data, Ncut aims at extracting the global impression of an image. It is assumed to be capable of utilizing the distinct global dissimilarities between target fluorophores and background AF in the whole fluorescence images to implement target/background segmentation. However, there are indeed more than two classes in the multispectral fluorescence images in the presence of multiple fluorophore targets. It is possible that the spectral emissions of some fluorescence targets are more similar to the AF spectral emission than other fluorescence targets. In this case, Ncut-based method will lead to a wrong target/background classification by grouping some fluorescence targets into the background AF group. To ensure accurate target/background classification, we modify classical Ncut method [23] to recursively repartition the large group of previous bipartition result if the number of groups segmented by Ncut is less than the number of endmembers in the fluorescence imaging. As a result, all the pixels of the multispectral images are classified into several groups, which further are simply merged into two main groups: the largest group is the background AF group and the rest of the smaller groups will join together into the target fluorescence group. Based on the improved Ncut-based classification, this paper has the following two contributions for the fluorescence SUM. First, by performing improved Ncut-based bipartitioning of target fluorescences and background AF groups, we propose target/background classification to benefit the endmember identification from the target and background groups for accurately initializing NMF. Second, this target/background classification facilitates imposing $L_{1/2}$ -norm [24], [25] partial sparseness constraint on the abundances of the target fluorescent group but not on that of AF group in the NMF, which is based on hierarchical alternating least squares (HALS) framework. The remainder of this paper is organized as follows. Section II describes the idea and the details of the proposed TBCR-NMF algorithm. Section III provides experimental results on synthetic and *in vivo* fluorescence imaging data. The conclusion and discussion are given in Section IV.

II. MATERIALS AND METHODS

The fluorescence image data acquired with multispectral imaging instruments comprise four contiguous bands in this paper. A multispectral data set is usually stacked as an image cube and thus can be treated as a 3-D volumetric data set with two spatial axes (X and Y) and one spectral axis (λ), as illustrated in Fig. 1. From a data-flow point of view, the flowchart of the proposed algorithm can be characterized as the following (see Fig. 1). First, a multispectral image cube is iteratively segmented into multiple separated homogeneous regions using the improved Ncut algorithm. Second, we further group these regions into target and background groups by classifying the largest region into the background group while merging all other small regions into the target group. Third, endmember extraction methods are employed to extract the spectral signatures \mathbf{S} of the target fluorescences and AF from the target and background regions for the NMF initialization.

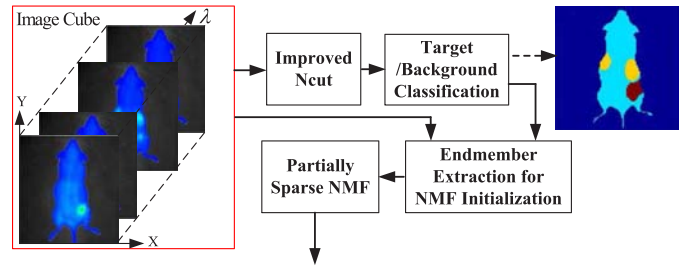


Fig. 1. Flowchart of the proposed TBCR-NMF algorithm.

Finally, NMF with partial sparseness constraint on the multiple target fluorescences is implemented to achieve the final SUM results.

A. Improved Ncut for Target/Background Classification

To distinguish the target fluorescence endmembers from AF endmember for accurately initializing NMF, we improved the classical Ncut [23] image segmentation method to globally classify the fluorescence image data into target and background groups. For the purpose of global target/background spatial segmentation, it may be inadequate to analyze multispectral image cube band by band or slice by slice using conventional local feature measures (entropy, variance, etc.) operating in the 2-D image space. Therefore, the whole multispectral image cube is considered as an image represented as a 2-D lattice of p -dimensional vectors (pixels), where $p = 4$ for our multispectral images acquired from four spectral bands. The space of the lattice is known as the spatial domain, while the multispectral fluorescence spectra are represented in the range domain.

According to the above definition and graph theory, the whole multispectral fluorescence image cube can be represented as a weighted undirected graph $\mathbf{G} = (\mathbf{V}, \mathbf{E})$, where the graph nodes \mathbf{V} are defined with pixels, with the spectrum vectors being normalized with zero-mean and unit variance, and the edges \mathbf{E} connect every pair of nodes. The weight $\mathbf{w}(i, j)$ on each edge represents the similarity between the nodes i and j . A graph can be optimally bipartitioned into two disjoint sets \mathbf{A} and $\mathbf{B} = \mathbf{V} - \mathbf{A}$ by removing the edges connecting the two parts, such that the intragroup similarity is high and the intergroup similarity is low. The degree of dissimilarity between these two sets, also called cut, is defined as $\text{cut}(\mathbf{A}, \mathbf{B}) = \sum_{u \in \mathbf{A}, v \in \mathbf{B}} \mathbf{w}(u, v)$ where u and v are nodes of the graph. The cut is equal to the total weight of the removed edges. The optimal bipartitioning of a graph is the one that minimizes this cut value. However, the criterion for finding the minimum cut always favors grouping small sets of isolated nodes in the graph, because the cut does not contain any intragroup information.

To get an unbiased optimal bipartition, Ncut [23] is proposed as a fraction of the total edge connections to all the nodes in the graph

$$\text{Ncut}(\mathbf{A}, \mathbf{B}) = \frac{\text{cut}(\mathbf{A}, \mathbf{B})}{\text{assoc}(\mathbf{A}, \mathbf{V})} + \frac{\text{cut}(\mathbf{A}, \mathbf{B})}{\text{assoc}(\mathbf{B}, \mathbf{V})} \quad (1)$$

where $\text{assoc}(\mathbf{A}, \mathbf{V}) = \sum_{u \in \mathbf{A}, t \in \mathbf{V}} \mathbf{w}(u, t)$ is the total connections from nodes in \mathbf{A} to all nodes in the graph and $\text{assoc}(\mathbf{B}, \mathbf{V})$ is similarly defined. The Ncut grouping algorithm consists of the following steps. First, let \mathbf{H} be an $N \times N$ diagonal matrix with \mathbf{h} on its diagonal and N be the number of the nodes and $\mathbf{h}(i) = \sum_j \mathbf{w}(i, j)$, where the weight $\mathbf{w}(i, j)$ is defined as $\mathbf{w}(i, j) = e^{-(\|\mathbf{x}_i - \mathbf{x}_j\|^2/\sigma)}$, with \mathbf{x}_i and \mathbf{x}_j representing the normalized spectra of nodes i and j , which have zero-mean and unit variance, respectively. In addition, $\sigma = 0.1$ is a positive scaling factor determining the sensitivity of $\mathbf{w}(i, j)$ to the spectrum difference between nodes i and j ; Then, we solve $(\mathbf{H} - \mathbf{W})\mathbf{v} = \eta\mathbf{H}\mathbf{v}$ for eigenvectors \mathbf{v} with the smallest eigenvalues η , where \mathbf{W} is $N \times N$ symmetric weight matrix with the element being $\mathbf{w}(i, j)$. At last, use the second smallest eigenvector \mathbf{v}_1 and the splitting value 0.4 to bipartition graph, i.e., the bipartition is implemented by grouping the i th node into \mathbf{A} if the i th component of eigenvector \mathbf{v}_1 is larger than 0.4, \mathbf{B} otherwise.

For the multiple fluorophores in *in vivo* fluorescence imaging, there are more than two classes in the fluorescence imaging. Therefore, the spectral emissions of some fluorescence targets are more similar to those of AF than other fluorescence targets, such that Ncut will lead to a wrong target/background classification by aggregating some fluorescence targets into the background AF group. To avoid this misclassification, we need to modify the recursive two-way Ncut method. Considering that background AF (including various background noises) has a dispersive spatial distribution while multiple fluorophores are locally accumulated at specific locations, we assume that the pure background AF regions are larger than the target fluorophore regions. Through Ncut-based bipartition, the larger group is either pure AF region or the regions that contain AF and some target fluorophores. In the latter case, the larger group will be bipartitioned again until all target fluorophores are separated from the AF region. Because the aim of the improved recursive Ncut method is to classify all pixels of the whole fluorescence region into two classes, background AF and target fluorescence groups, all the separated smaller regions except the largest AF region are finally combined together into the target fluorescence group.

Based on the above analysis, we propose an improved recursive Ncut method. First, to use the Ncut method, each 992×992 spectral image is decimated into a size of 100×100 pixels. Decreasing the number of graph nodes from near $N = 1\,000\,000$ to $N = 10\,000$ by this image subsampling can solve the large graph problem, which consumes too much memory and requires huge computational complexity in handling large-scale weight matrix \mathbf{W} (with $N \times N$ elements) for the graphical representation and generalized eigenvalue computation. In our experiments, changing image size from 200×200 pixels to 100×100 pixels can obviously decrease Ncut computation time from 50.6 to 2.8 s, but does not have an adverse effect on target/background classification, because the Ncut method's graph-based generalized eigenvalue computation is less sensitive to the spatial information lost during subsampling than other local feature-based segmentation. Besides, even if small noisy misclassification occurs, it cannot

affect the final TBCR-NMF's performance, because we only require an approximate global target/background classification for further decomposition refinement by TBCR-NMF itself. Second, after the initial Ncut-based bipartition, only the large cluster of the bipartition result will be chosen for subsequent bipartition. Third, we recursively repartition the large cluster of previous bipartition result if the number of intermediate clusters segmented by Ncut is less than the number of endmembers in the fluorescence imaging. Finally, the largest group is considered as the background AF group and all the rest of smaller groups are merged into the target fluorescence group. The intermediate target/background classification result after improved Ncut segmentation is shown in Fig. 1, where the different colors mean the different intermediate clusters sequentially segmented by the improved Ncut. The final target fluorescence group is formed by grouping all the small clusters except the large cluster of AF region.

B. Endmember Extraction for NMF Initialization

To find the optimal product \mathbf{CS} that best approaches the mixed image data matrix $\mathbf{D} \in \mathbb{R}_+^{N \times L}$ (N is the total pixel number in a single image and L is the spectral band number), HALS-based NMF [26]–[28] is adopted to perform sequential constrained minimization on a set of subobjective functions $F(\mathbf{C}_{:k}, \mathbf{S}_{k:}) = (1/2)\|\mathbf{R}_k - \mathbf{C}_{:k}\mathbf{S}_{k:}\|_2^2$, where each column $\mathbf{C}_{:k}$ of $\mathbf{C} \in \mathbb{R}_+^{N \times K}$ represents the spatial distribution of one endmember component, K is the number of the endmember, and each row $\mathbf{S}_{k:}$ of $\mathbf{S} \in \mathbb{R}_+^{K \times L}$ represents the spectrum of a specific endmember. for $k = 1, 2, \dots, K$, $\mathbf{R}_k = \mathbf{D} - \sum_{i \neq k} \mathbf{C}_{:i}\mathbf{S}_{i:}$.

To initialize NMF, we use the pixels of two groups to determine the corresponding spectra for the different fluorescence components. We assume that the first $(K - 1)$ constituent components represent the fluorophores and the last component describes the AF. AF's initialized spectrum (\mathbf{S}_K) is set to the average spectrum of all AF pixels, while the spectra $\mathbf{S}_1, \mathbf{S}_2, \dots, \mathbf{S}_{K-1}$ can be set by the endmember extraction method, i.e., automatic target generation process (ATGP) [29], which searches the most distinctive pixels in the target fluorescence group with the orthogonal subspace projection approach. To remove the residual AF effect on the fluorescence targets, we subtract the average AF intensity \mathbf{S}_K from each band's data in the fluorescence target group before using the ATGP to obtain the endmember spectra of fluorophores. At last, the abundance matrix \mathbf{C} can be initialized by fixing the spectra \mathbf{S} during the initial ten iterations of NMF.

C. Partially Sparse NMF

A sparseness constraint is helpful in improving signal decomposition uniqueness along with enforcing a local-based representation [30]. To implement L_p ($0 < p < 1$)-norm based sparseness constraint that can give stronger sparse NMF solutions [24], [25] than the L_1 -norm [10], we impose the $L_{1/2}$ -norm sparseness constraint on the abundances of multiple fluorophores. For $k = 1, 2, \dots, K - 1$, we propose the subobjective function of HALS-based NMF with

the $L_{1/2}$ -norm as

$$F(\mathbf{C}_{:k}, \mathbf{S}_{k:}) = \frac{1}{2} \|\mathbf{R}_k - \mathbf{C}_{:k} \mathbf{S}_{k:}\|_2^2 + 2\theta \sum_{i=1}^N (\mathbf{C}_{ik})^{1/2} \quad (2)$$

where the θ is a regularized parameter to balance the tradeoff between the approximation accuracy and the sparseness of the multiple fluorophores' abundances. The gradient derivation of $F(\mathbf{C}_{:k}, \mathbf{S}_{k:})$ with respect to $\mathbf{C}_{:k}$ is

$$\frac{\partial F(\mathbf{C}_{:k}, \mathbf{S}_{k:})}{\partial \mathbf{C}_{:k}} = -(\mathbf{R}_k - \mathbf{C}_{:k} \mathbf{S}_{k:}) \mathbf{S}_{k:}^T + \theta (\mathbf{C}_{:k})^{-1/2} \quad (3)$$

where $\mathbf{C}_{:k}^{-1/2}$ is given by the element-wise square root for each entry in the vector $\mathbf{C}_{:k}$. By setting (3) to zero, we can get the updating rule of $\mathbf{C}_{:k}$. However, it involves a rather high computation cost due to the computation of the term $\mathbf{C}_{:k}^{-1/2}$. To circumvent this problem, we approximate $\mathbf{C}_{:k}$ in the $\theta (\mathbf{C}_{:k})^{-1/2}$ term by its estimation $\hat{\mathbf{C}}_{:k}$ obtained from the previous update, rather than compute the term $\mathbf{C}_{:k}$ directly. Hence, (3) takes a simplified and more computationally efficient form

$$\frac{\partial F(\mathbf{C}_{:k}, \mathbf{S}_{k:})}{\partial \mathbf{C}_{:k}} = -(\mathbf{R}_k - \mathbf{C}_{:k} \mathbf{S}_{k:}) \mathbf{S}_{k:}^T + \theta \hat{\mathbf{C}}_{:k}^{-1/2}. \quad (4)$$

By setting (4) to zero, the rule of updating $\mathbf{C}_{:k}$ takes the following form:

$$\mathbf{C}_{:k} = \max(\text{eps}, (\mathbf{R}_k \mathbf{S}_{k:}^T - \theta (\mathbf{C}_{:k})^{-1/2}) / \|\mathbf{S}_{k:}\|_2^2) \quad (5)$$

where eps is a very small constant ($\sim 10^{-16}$) and prevents from dividing by zero. The rules of updating $\mathbf{S}_{k:}$ for (2) is

$$\mathbf{S}_{k:} = \max(\text{eps}, \mathbf{C}_{:k}^T \mathbf{R}_k / \|\mathbf{C}_{:k}\|_2^2). \quad (6)$$

For $k = K$, the subobjective function has no sparseness constraint, and the corresponding updating rules are the same as the other parts of the HALS optimization.

For the convenience of parameter setting, we convert the regularized parameter θ of TBCR-NMF into a desired sparsity value ϕ [10], which represents the sparseness degree that we expect the abundances of multiple fluorophores to reach. The sparsity value ϕ , being 0 for nonsparse results and 1 for extremely sparse results, can be defined as

$$\phi(\mathbf{C}_k) = \frac{\sqrt{N} - (\sum_{n=1}^N |\mathbf{c}_{nk}| / \sqrt{\sum_{n=1}^N \mathbf{c}_{nk}^2})}{\sqrt{N} - 1} \quad (7)$$

where $\mathbf{C}_k \in \mathbb{R}_+^{N \times 1}$ is the k th column of abundance matrix \mathbf{C} , and \mathbf{c}_{nk} is each element at \mathbf{C}_k with $n = 1, 2, \dots, N$. Specifically, for each fluorophore's abundance $\mathbf{C}_{:k}$ that has a corresponding regularized parameter θ_k , we use a method similar to that in [31] to directly control the θ_k value: θ_k is initialized to 0.001, and after each iteration, the current sparsity ϕ is computed by (7) for the abundance $\mathbf{C}_{:k}$; then θ_k is increased by 5% if the current sparsity is less than the desired sparsity value ϕ ; otherwise, θ_k is decreased by 5%.

The detailed pseudocode of partially sparse NMF algorithm is summarized in Algorithm 1. The algorithm computation is terminated when the absolute value of difference between the two adjacent objective functions is less than 10^{-4} , or the maximum number of iterations exceeds 1000.

Algorithm 1 Partially Sparse NMF

Input: Data matrix $\mathbf{D} \in \mathbb{R}_+^{N \times L}$ and initial $\mathbf{C} \in \mathbb{R}_+^{N \times K}$ and $\mathbf{S} \in \mathbb{R}_+^{K \times L}$ and ϕ

Output: \mathbf{C}, \mathbf{S}

```

1 for  $k = 1$  to  $K - 1$  do
2   |  $\theta_k = 0.001$ ;
3 end
4 while stopping criterion not satisfied do
5   for  $k = 1$  to  $K$  do
6     | if  $k < K$  then
7       |  $\mathbf{C}_{:k} = \max(\text{eps}, (\mathbf{R}_k \mathbf{S}_{k:}^T - \theta_k (\mathbf{C}_{:k})^{-1/2}) / \|\mathbf{S}_{k:}\|_2^2)$ ;
8       | if Sparsity( $\mathbf{C}_{:k}$ )  $> \phi$  then
9         | |  $\theta_k = 0.95\theta_k$ ;
10        | else
11        | |  $\theta_k = 1.05\theta_k$ ;
12        | end
13       | else
14       | |  $\mathbf{C}_{:k} = \max(\text{eps}, \mathbf{R}_k \mathbf{S}_{k:}^T / \|\mathbf{S}_{k:}\|_2^2)$ ;
15       | end
16       |  $\mathbf{S}_{k:} = \max(\text{eps}, \mathbf{C}_{:k}^T \mathbf{R}_k / \|\mathbf{C}_{:k}\|_2^2)$ ;
17       | where  $\mathbf{R}_k = \mathbf{D} - \sum_{i \neq k} \mathbf{C}_i \mathbf{S}_i$ ;
18     | end
19 end
```

III. RESULTS

We first use synthetic data to evaluate the performance of TBCR-NMF algorithm by comparing TBCR-NMF with HALS-based NMF with L_1 sparseness constraint (L_1 -HALS) [26] and sparse NMF (S-NMF) [4]. L_1 -HALS introduces the sparseness constraint into all abundances, while S-NMF uses dynamic threshold to add the sparseness constraint into the abundances of multiple fluorophores. L_1 -HALS has θ , while S-NMF has ϕ to control the sparseness degree in NMF. S-NMF initializes the endmember spectra \mathbf{S} with the calibrated spectra through calibration experiment in advance [4]. Therefore, we regard S-NMF as a *Pure* method and TBCR-NMF as a *Graph* method, while L_1 -HALS with random initialization is a *Random* method. Both *Graph* and *Random* methods do not use *a priori* knowledge of calibrated endmember spectra, while the *Pure* method needs the calibrated endmember spectra.

To evaluate the performances of the different algorithms, the spectral angle distance (SAD) [32] is defined to measure the angle (or similarity) between the k th true endmember signature \mathbf{S}_k and its estimate $\hat{\mathbf{S}}_k$

$$\text{SAD}_k = \arccos\left(\frac{\mathbf{S}_k \hat{\mathbf{S}}_k^T}{\|\mathbf{S}_k\|_2 \|\hat{\mathbf{S}}_k\|_2}\right). \quad (8)$$

Furthermore, root mean square error (RMSE) [33] is taken to evaluate the similarity between the true and estimated abundances

$$\text{RMSE}_k = \sqrt{\frac{1}{N} \sum_{i=1}^N (\mathbf{C}_{ki} - \hat{\mathbf{C}}_{ki})^2}. \quad (9)$$

In general, the smaller value of SAD (or RMSE) means the better similarity and better unmixing performance of NMF. At last, the average SAD ($\overline{\text{SAD}}$) and RMSE ($\overline{\text{RMSE}}$) for

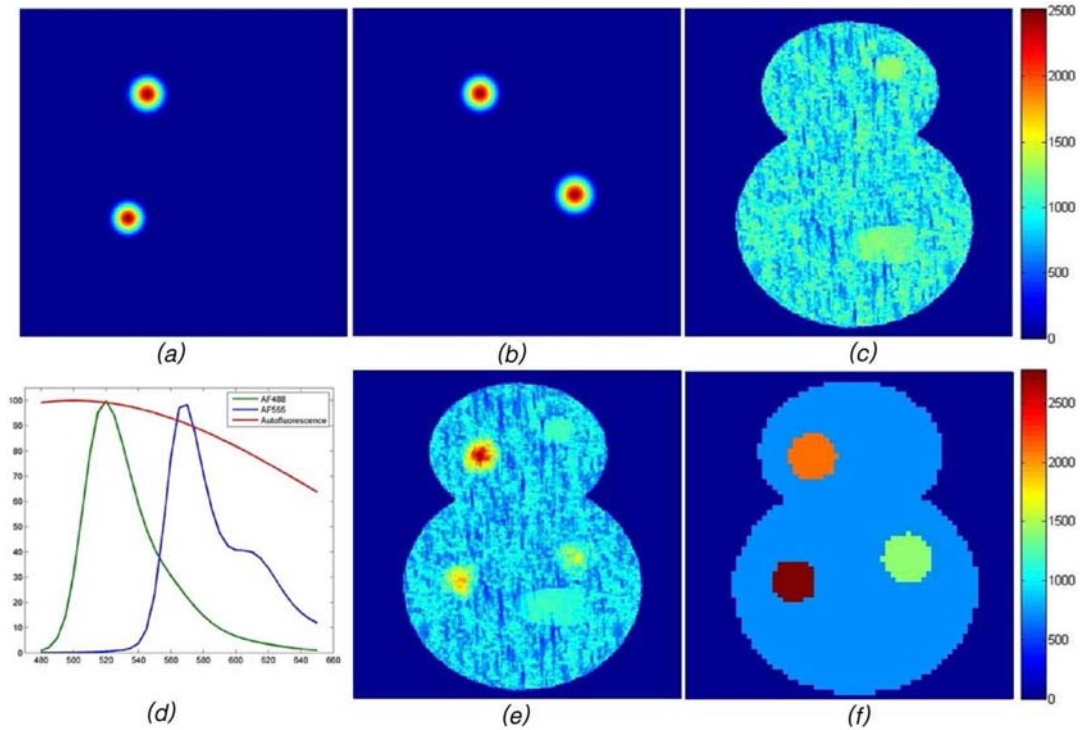


Fig. 2. Synthetic Data. (a)–(c) Abundances of AF488, AF555, and AF. (d) Corresponding emission spectra for AF488 (green line), AF555 (blue line), and AF (red line). (e) Mixed fluorescence image acquired at 555 nm. (f) Grouping result obtained with improved Ncut target/background classification.

all endmember components are used to evaluate the overall performance of estimating spectral signatures and their corresponding abundances, respectively.

A. Synthetic Data

We use two fluorescence parts, Alexa Fluor 488 and Alexa Fluor 555 (AF488, AF555; Invitrogen, Carlsbad, USA), and one AF part to build a simulated phantom [4] in Fig. 2. The spectral signatures of fluorescence parts are fitted emission spectral curves of AF488 and AF555 at the spectral wavelengths from 480 nm to 650 nm with interval of 5 nm, while AF's spectral signature is a slowly varying curve in the same range [see Fig. 2(d), green line for AF488, blue line for AF555, and red line for AF]. The abundances of AF488 and AF555 consist of two parts: one part is pure fluorescence dye and the other part is mixed with AF488 and AF555 [see Fig. 2(a) and (b)]. The mixed part is at the top-left of the phantom, while the pure parts are at the bottom-left for AF488 in Fig. 2(a) and the bottom-right for AF555 in Fig. 2(b). According to the sparsity definition in (7), the true sparsity of the abundance of AF488 (or AF555) is 0.85. Finally, the total simulated phantom is obtained by adding the two fluorescence parts and the AF part together, and the abundance intensity ratio of AF to fluorophores (AF/F intensity ratio) is 0.3. Fig. 2(e) shows the mixed fluorescence image acquired at the spectral band of 555 nm wavelength. Fig. 2(f) shows the classification result of the synthetic data. The target fluorescence group is obtained by combining three different fluorescence regions (with different colors), which are

sequentially isolated from the background AF group after three iterations of the improved recursive Ncut computation.

We test the above-mentioned algorithms' unmixing performances with the metrics of $\overline{\text{SAD}}$ and $\overline{\text{RMSE}}$, which have averages (bars) and standard deviations (error bars) resulting from the 20 runs of each algorithm. The algorithms' performances are dependent on the initial sparsity parameter ϕ (or the regularized parameter θ). Too small values of ϕ and θ cannot represent a reasonable sparsity of unmixed results while too large values of ϕ and θ will lead to excessive sparsity and inaccurate unmixed results. Considering the general sparsity of abundances for multiple fluorophores in preclinical applications, we select a series of ϕ values from 0.5 to 0.9 with an interval of 0.05 to demonstrate the effects of different initial sparsity values on the performance of S-NMF and TBCR-NMF. As for L_1 -HALS, the θ value is 10^{-4} , 5×10^{-4} , 10^{-3} , 5×10^{-3} , 0.01, 0.05, 0.1, 0.5, and 1.0.

The performance metrics for different parameters of θ and ϕ are shown in Fig. 3 when the AF/F intensity ratio is set to 0.3 with no noise added and with signal-to-noise ratio (SNR) being set to $\text{SNR} = 15$ dB. L_1 -HALS's performance has been influenced by the regularized parameter θ . The $\overline{\text{SAD}}$ and $\overline{\text{RMSE}}$ achieved with L_1 -HALS are the largest compared with other algorithms. For S-NMF and TBCR-NMF, their unmixing performances also have been influenced by the different values of initial sparsity parameter ϕ , which should be set to the true sparsity (0.85) of the abundance of multiple fluorophores in ideal situations. Therefore, too small or too large ϕ cannot produce good unmixed results for S-NMF and TBCR-NMF. In Fig. 3(a), when ϕ is smaller than 0.65 or larger

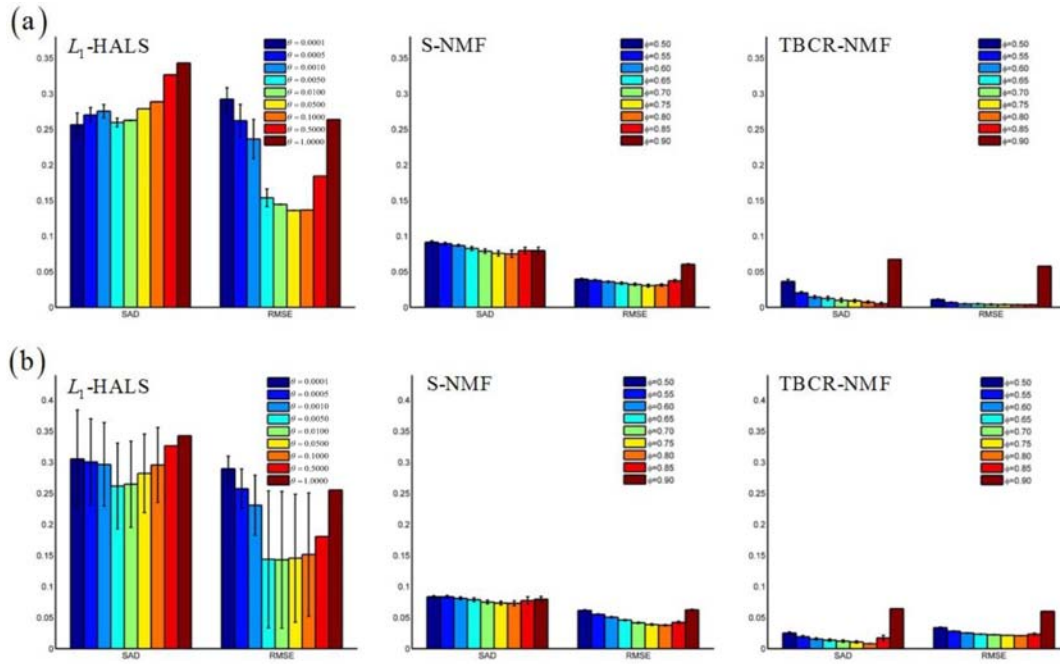


Fig. 3. Algorithm performances ($\overline{\text{SAD}}$ and $\overline{\text{RMSE}}$) for different values of parameter θ and ϕ when (a) no noise is added and (b) noise is added with SNR = 15 dB.

than 0.85, the $\overline{\text{SAD}}$ and $\overline{\text{RMSE}}$ become large and the unmixed results obtained with S-NMF and TBCR-NMF become worse. However, TBCR-NMF obtains the smallest $\overline{\text{SAD}}$ and $\overline{\text{RMSE}}$ among the three algorithms when the sparsity ϕ changes from 0.50 to 0.90 (or θ changes from 0.0001 to 1.0000). When the sparsity ϕ value is set to 0.90 (or θ changes from 0.0001 to 1.0000), the poorest performances are achieved by all three algorithms, among which the TBCR-NMF is still the best.

The SNR in Fig. 3(b) is set to 15 dB, so that there is strong noise in the fluorescence data and the performance of all algorithms degrades with increasing noise levels. The proposed TBCR-NMF still achieves the smallest $\overline{\text{SAD}}$ and $\overline{\text{RMSE}}$ when ϕ ranges from 0.5 to 0.9. The RMSE achieved by TBCR-NMF is relatively steady when ϕ ranges from 0.5 to 0.85. When the initial sparsity value ϕ exceeds the true sparsity (0.85), the values of $\overline{\text{SAD}}$ and $\overline{\text{RMSE}}$ obtained by TBCR-NMF increase obviously, but are still smaller than those obtained by other algorithms. Therefore, TBCR-NMF can achieve the best unmixed results when there is strong noise in the fluorescence data.

As low AF/F ratio will highlight multiple localized fluorophores from the background AF, it essentially makes the mixed spectral data sparser than the high AF/F ratio and the corresponding NMF problem will have sparser solutions than the high AF/F ratio. Therefore, the NMF performance is largely dependent on the AF/F ratio. For simulation experiments, the AF/F intensity ratio ranges from 0.1 to 0.9 with interval of 0.2. The ϕ and θ parameters are set to 0.8 and 0.01, respectively, to achieve the best unmixing performance for all algorithms.

Fig. 4(a) shows the different $\overline{\text{SAD}}$ and $\overline{\text{RMSE}}$ values for the different AF/F intensity ratios in the noiseless data. The initialization is *Random* method for L_1 -HALS, *Pure* method

for S-NMF, and *Graph* method for TBCR-NMF. Fig. 4(a) shows that the performances of L_1 -HALS and S-NMF algorithms improve with decreasing AF/F intensity ratio. The unmixed results obtained with L_1 -HALS are worst compared with other results. However, TBCR-NMF is not sensitive to the AF/F ratio and obtains the smallest $\overline{\text{SAD}}$ and $\overline{\text{RMSE}}$ values in all different AF/F intensity ratios.

Fig. 4(b) shows the performance dependence on the different initialization methods, when AF/F ratio, ϕ and θ , are set to 0.3, 0.8, and 0.001, respectively. L_1 -HALS is initialized with *Random*, *Graph*, and *Pure* methods, while S-NMF and TBCR-NMF are initialized with *Graph* and *Pure* methods. The $\overline{\text{SAD}}$ and $\overline{\text{RMSE}}$ values of L_1 -HALS using different initializations are similar and the worst among the three algorithms due to the sparseness constraint being imposed on all abundances. S-NMF's performance improves with the *Pure* initialization having *a priori* knowledge of calibrated endmember spectra compared with the *Graph* initialization without *a priori* knowledge, while the TBCR-NMF can obtain the best unmixed results in both initialization methods even without *a priori* knowledge of calibrated spectra.

B. In Vivo Experiment I

In this section, we apply the proposed algorithm to *in vivo* fluorescence data acquired by the Bio-Real Quick View 3000 (Bio-Real Sciences, Austria) system, which is an epillumination planar imaging system equipped with electron multiplying charge coupled device (EMCCD) and the light source of 150 W Xenon arc lamp. In the sparse acquisition of fluorescence imaging for this work, the EMCCD (Andor Technology, Ireland, DU885) gets the fluorescence image (992×992 pixels) through four bandpass (30 nm width) emission filters (Semrock, Rochester, USA).

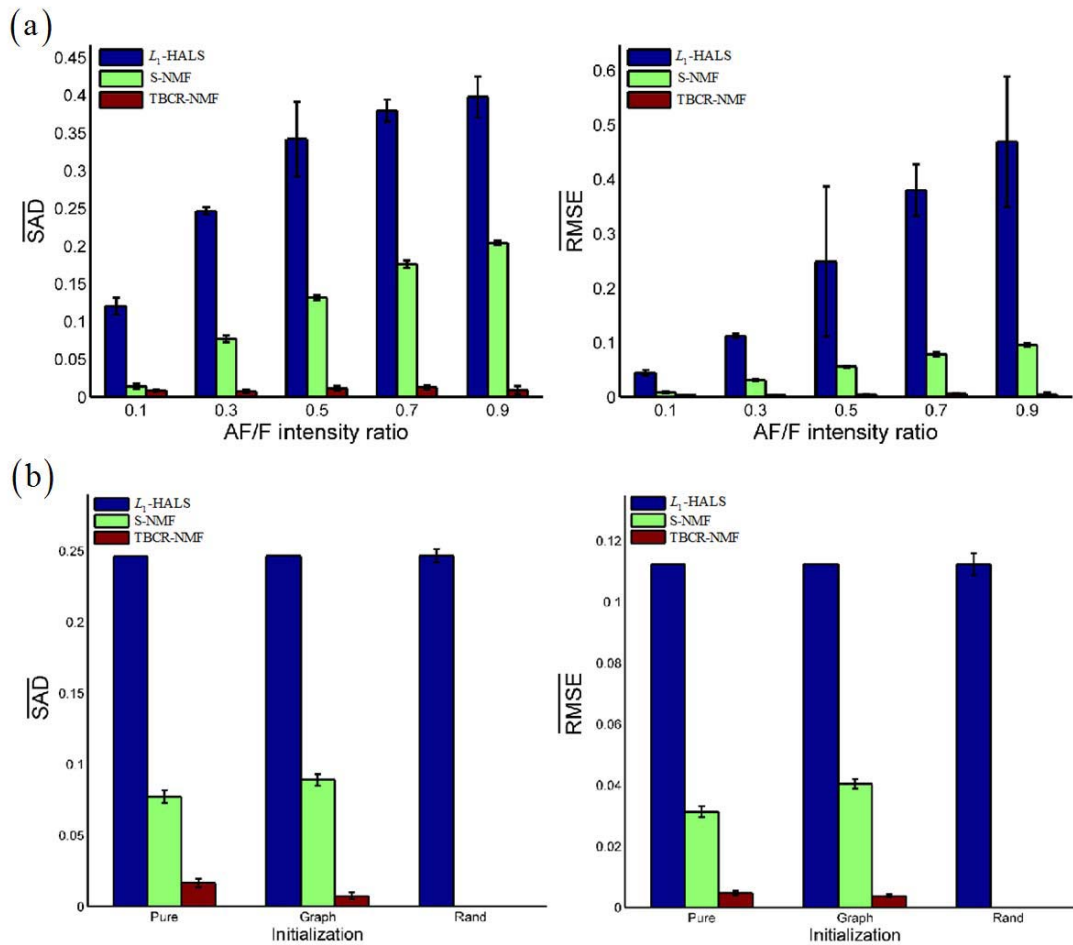


Fig. 4. (a) Algorithm performances for different values of AF/F intensity ratio. (b) Algorithm performances for different initialization methods.

Besides the L_1 -HALS and S-NMF, we also use two NMF-based SUM algorithms: nonnegative matrix underapproximation (NMU)² [34] and NMF with L_0 constraint (L_0 -NMF) [35] for comparison. NMU solves NMF problem with additional underapproximation constraint $\mathbf{CS} \leq \mathbf{D}$ which allows to obtain better part-based decompositions, while L_0 -NMF introduces sparseness into all abundances via the L_0 -norm constraint. All algorithms assume that the number of endmembers is 3, or $K = 3$. The TBCR-NMF, L_1 -HALS, NMU, and L_0 -NMF methods are not initialized with *a priori* knowledge of calibrated endmember spectra except the S-NMF method. The parameter ϕ for L_0 -NMF, S-NMF, and TBCR-NMF is 0.75, the parameter θ for L_1 -HALS is 0.005. To reduce computation cost, we use Otsu's [36] method for preprocessing to obtain the mouse body mask with whole fluorescence regions of interest, whereby all algorithms are applied to the fluorescence data within the mask only. For the best visual effect, all the observations and unmixed results (spatial distribution of all constituent components) are shown with rainbow pseudocolor and overlaid on the gray-scale photographic image of corresponding mouse.

We first give two *in vivo* BALB/c mouse experimental results to validate the proposed method's performance.

All animal experiments in this paper were approved by our institutional review board. In experiment I, AF488 and Alexa Fluor 594 (AF594; Invitrogen, Carlsbad, USA) fluorescent dyes are diluted to $0.1 \mu\text{gml}^{-1}$. AF488 is injected at the bottom of the body with 20 ng dye, while AF594 is injected near the neck with the same quantity, and a mixture of each dye with 10 ng is located at the middle portion of the body. These three injections are not exactly controlled with the same depth in tissues. Fig. 5(a)–(d) shows four raw fluorescence images acquired at 542, 579, 624, and 716 nm spectral bands. The first two images are excited at 474 nm and the last two images at 565 nm. The calibrated spectra of AF488, AF594, and AF [see Fig. 6(a)] are acquired at these four emission filters by precalibration *ex vivo* experiments in the same imaging conditions, while the spectrum of AF is the average spectrum acquired in some chosen regions of mouse with no fluorescent dyes. Fig. 6(a) displays that AF488, AF594 and AF have overlapping emission spectra. Fig. 6(b) and (c) also shows the calibrated spectra of AF488, AF555, and AF, acquired *ex vivo* at the 525, 542, 579, and 624 nm spectral bands for the next two *in vivo* fluorescence imaging experiments in the following section.

Fig. 5(e) shows the target/background classification result where the multiple fluorophores are classified as a target group (red color) and separated from the whole background

²<https://sites.google.com/site/nicolasgillis/code>

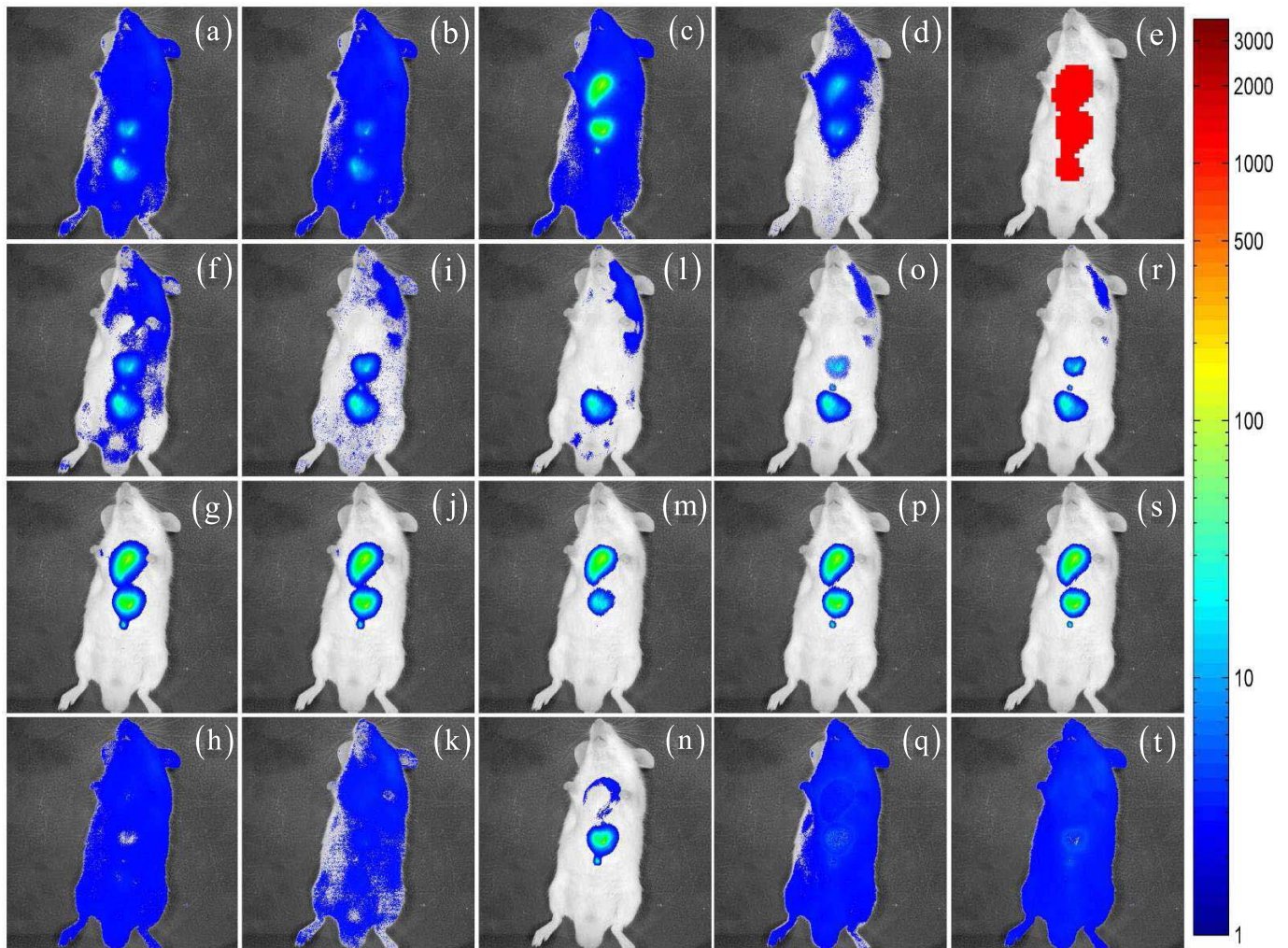


Fig. 5. (a)–(d) Raw fluorescence (AF488 and AF594) images for experiment I acquired at the 542, 579, 624, and 716 nm emission filters; the first two images are excited at 474 nm and the last two images at 565 nm. (e) Classification results obtained by improved recursive Ncut method. The different unmixed results obtained by (f)–(h) NMU, (i)–(k) L_0 -NMF, (l)–(n) L_1 -HALS, (o)–(q) S-NMF, and (r)–(t) TBCR-NMF.

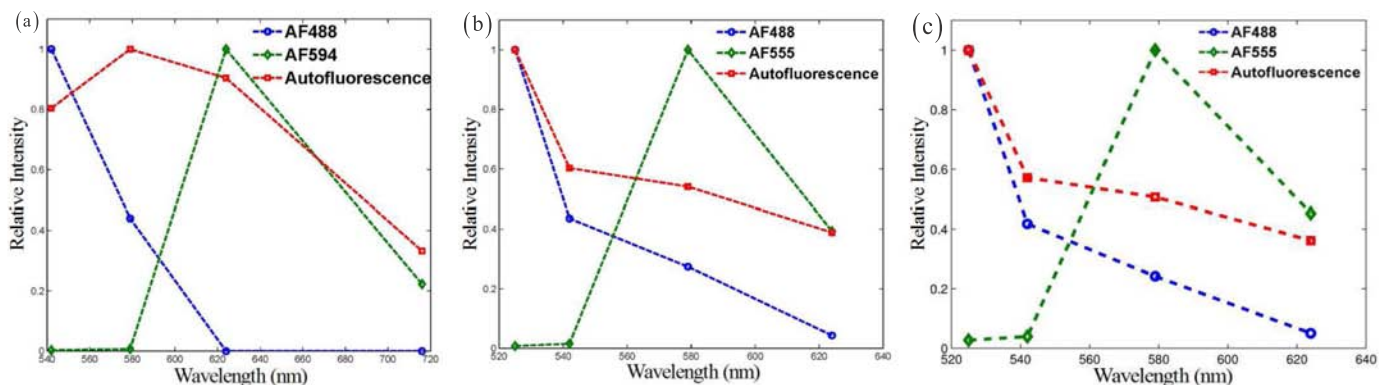


Fig. 6. (a) Spectra of AF488 and AF594 for experiment I acquired *ex vivo* at the 542, 579, 624, and 716 nm spectral bands, and average spectrum of AF acquired from mouse. (b) Spectra of AF488 and AF555 for experiment II acquired *ex vivo* at the 525, 542, 579, and 624 nm spectral bands, and average spectrum of AF acquired from mouse. (c) Spectra of AF488 and AF555 for experiment III acquired *ex vivo* at the 525, 542, 579, and 624 nm spectral bands, and average spectrum of AF acquired from mouse.

AF group. The unmixed results (abundances expressed as 2-D images) of BALB/c mouse by NMU are illustrated in Fig. 5(f)–(h), L_0 -NMF in Fig. 5(i)–(k), L_1 -HALS

in Fig. 5(l)–(n), S-NMF in Fig. 5(o)–(q), and TBCR-NMF in Fig. 5(r)–(t). The fluorescence targets are still mixed with AF in Fig. 5(f) by NMU and in Fig. 5(i) by L_0 -NMF.

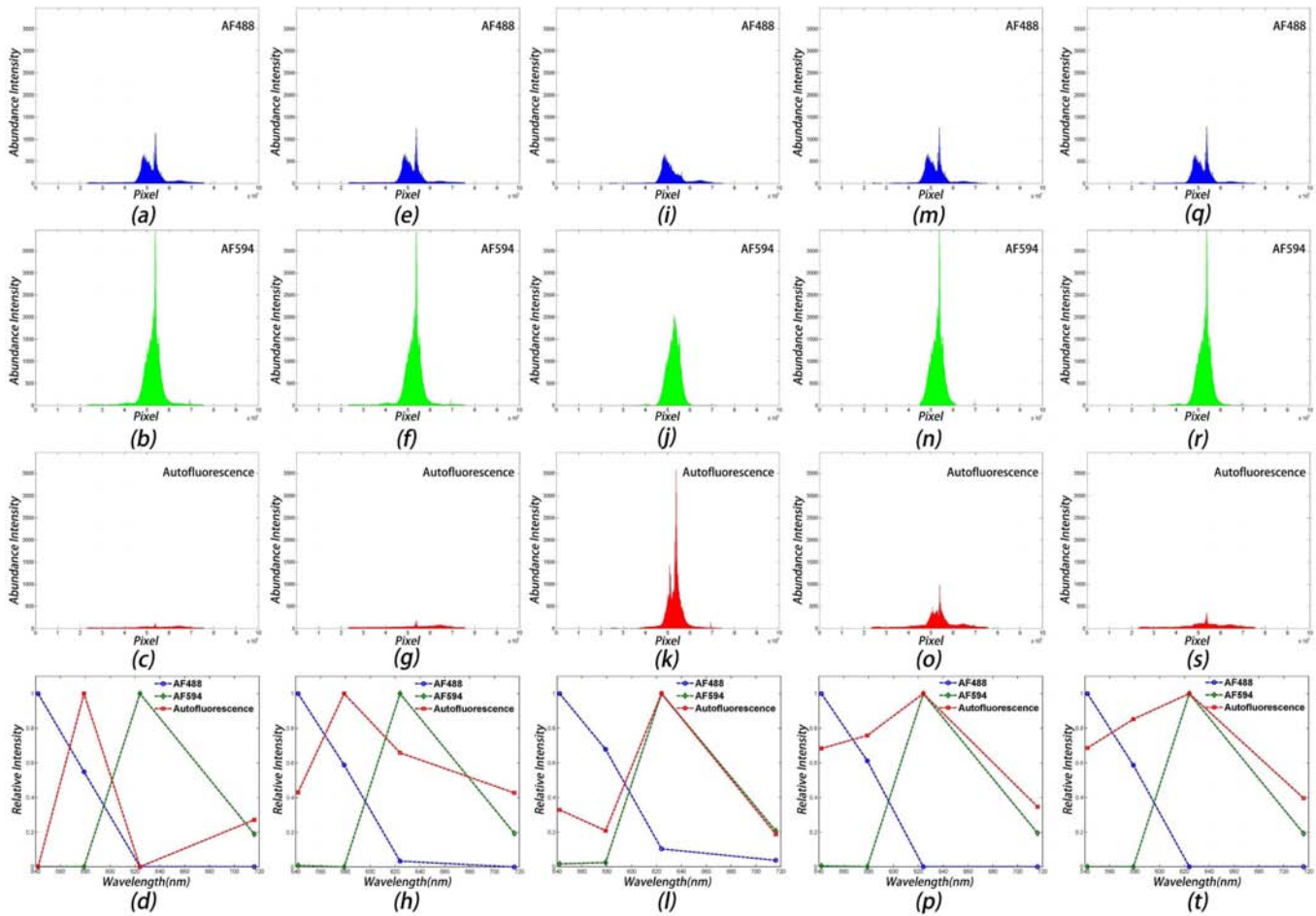


Fig. 7. Abundances (expressed as 1-D vectors) \mathbf{C} of AF488, AF594, AF, and their spectra \mathbf{S} from top row to bottom row for experiment I. The unmixed results obtained with (a)–(d) NMU, (e)–(h) L_0 -NMF, (i)–(l) L_1 -HALS, (m)–(p) S-NMF, and (q)–(t) TBCR-NMF.

There are some missing parts of AF488 in the middle portion of BALB/c mouse in Fig. 5(l) for L_1 -HALS, which also falsely makes the unmixed background AF [Fig. 5(n)] appear sparser and brighter than it actually is. The TBCR-NMF and S-NMF can separate the fluorescence targets from AF in Fig. 5(o)–(q) and Fig. 5(r)–(t), respectively. However, the unmixed results obtained with TBCR-NMF are smoother and clearer than S-NMF.

The unmixed results of abundances \mathbf{C} (expressed as 1-D vectors) and endmember spectra \mathbf{S} are illustrated in Fig. 7(a)–(d) for NMU, Fig. 7(e)–(h) for L_0 -NMF, Fig. 7(i)–(l) for L_1 -HALS, Fig. 7(m)–(p) for S-NMF and Fig. 7(q)–(t) for TBCR-NMF, respectively. The TBCR-NMF algorithm obtains more accurate unmixed fluorescence abundances compared with the other algorithms. All algorithms have the highest abundance intensities that correspond to the true pixel positions of fluorescence targets. The abundances of AF488 and AF594 are wide and contain the unwanted AF parts that are not removed with NMU in Fig. 7(a) and (b) and L_0 -NMF in Fig. 7(e) and (f). This AF remainder also can be confirmed by AF's abundances [Fig. 7(c) and (g)] obtained with both algorithms. The L_1 -HALS [Fig. 7(k)] and S-NMF [Fig. 7(o)] have abnormal (too large) values in the abundances of AF, except that

the TBCR-NMF [Fig. 7(s)] has slowly varying abundances of AF. More importantly, the spectra estimated with S-NMF [Fig. 7(p)] and TBCR-NMF [Fig. 7(t)] are much more similar to the true calibrated ones [Fig. 5(a)] than other algorithms.

The SAD and $\overline{\text{SAD}}$ values of three unmixed endmembers for *in vivo* experiment I are shown in Table I. The smaller the SAD (or $\overline{\text{SAD}}$) value, the better the unmixed results. The average $\overline{\text{SAD}}$ values of all three endmembers represent the overall performances of all unmixing methods. Therefore, TBCR-NMF achieves the smallest $\overline{\text{SAD}}$ (0.0943) and the best unmixing accuracy.

C. In Vivo Experiment II

In experiment II, we use the AF488 and AF555 as two fluorophores whose spectra are overlapped with each other and with that of the AF [see Fig. 6(b)]. The AF488 and AF555 fluorescent dyes are diluted to $0.1 \mu\text{gml}^{-1}$. AF488 is subcutaneously injected at the bottom-right of the body with 50 ng dye and AF555 is subcutaneously injected on the left and right sides of body's middle portion with 50 ng dye. The raw fluorescence images acquired at the 525, 542, 579, and 624 nm emission filters are displayed in Fig. 8(a)–(d).

Fig. 8(e) shows the target/background classification separating the AF and red target fluorescence groups.

TABLE I
SAD AND $\overline{\text{SAD}}$ RESULTS ON THE *In Vivo* EXPERIMENTS I AND II (THE SMALLER VALUES MEAN BETTER RESULTS. THE NUMBER IN BOLD REPRESENTS THE BEST PERFORMANCE)

| Methods | p priori knowledge | Experiment I | | | | Experiment II | | | |
|-------------|--------------------|--------------|--------|--------|-------------------------|---------------|--------|--------|-------------------------|
| | | AF488 | AF594 | AF | $\overline{\text{SAD}}$ | AF488 | AF555 | AF | $\overline{\text{SAD}}$ |
| NMU | no | 0.0873 | 0.0339 | 0.8557 | 0.3256 | 0.1158 | 0.1853 | 0.4385 | 0.2466 |
| L_0 -NMF | no | 0.1209 | 0.0294 | 0.2559 | 0.1354 | 0.0973 | 0.3970 | 0.1335 | 0.2099 |
| L_1 -HALS | no | 0.2024 | 0.0258 | 0.6032 | 0.2771 | 0.1654 | 0.4243 | 0.0189 | 0.2029 |
| S-NMF | yes | 0.1343 | 0.0283 | 0.1654 | 0.1093 | 0.1167 | 0.2097 | 0.0160 | 0.1141 |
| TBCR-NMF | no | 0.1290 | 0.0278 | 0.1261 | 0.0943 | 0.0588 | 0.2060 | 0.0234 | 0.0961 |

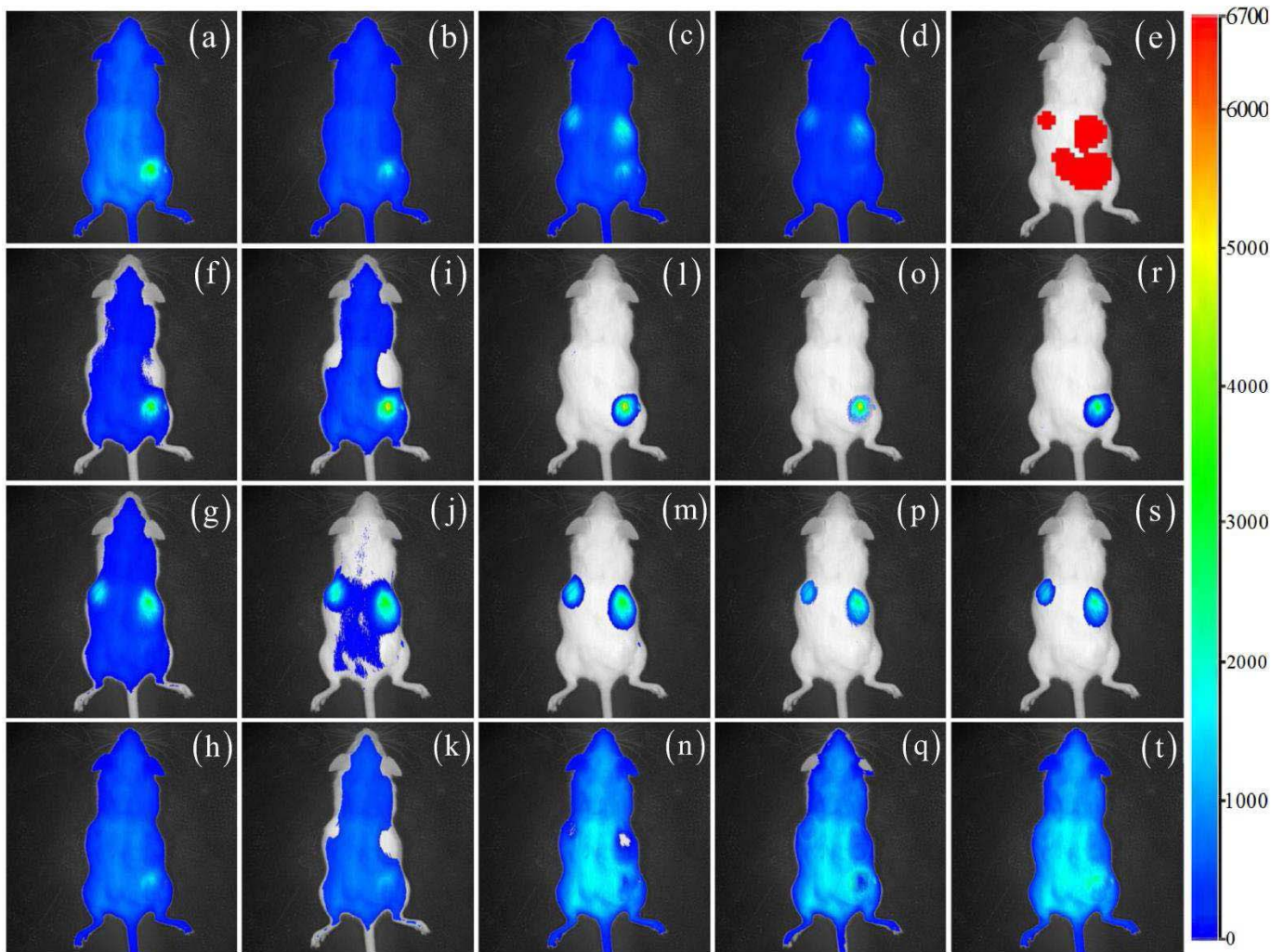


Fig. 8. (a)–(d) Raw fluorescence (AF488 and AF555) images for experiment II acquired at the 525, 542, 579, and 624 nm emission filters, the first two images are excited at 474 nm and the last two images at 500 nm. (e) Classification results. The different unmixed results obtained with (f)–(h) NMU, (i)–(k) L_0 -NMF, (l)–(n) L_1 -HALS, (o)–(q) S-NMF, and (r)–(t) TBCR-NMF.

Based on this classification, the unmixed results (abundances expressed as 2-D images) for BALB/c mouse are illustrated in Fig. 8(f)–(h) for NMU, Fig. 8(i)–(k) for L_0 -NMF, Fig. 8(l)–(n) for L_1 -HALS, Fig. 8(o)–(q) for S-NMF, and Fig. 8(r)–(t) for TBCR-NMF. AF488 and AF555 are not separated from AF by NMU in Fig. 8(f) and (g) and L_0 -NMF

in Fig. 8(i) and (j). L_1 -HALS, S-NMF, and TBCR-NMF can separate the two fluorescence targets from AF in Fig. 8(l)–(n), Fig. 8(o)–(q), and Fig. 8(r)–(t), respectively. But there are missing parts of AF in Fig. 8(n) with L_1 -HALS and Fig. 8(q) with S-NMF. The TBCR-NMF method can estimate the best unmixed results compared with other algorithms.

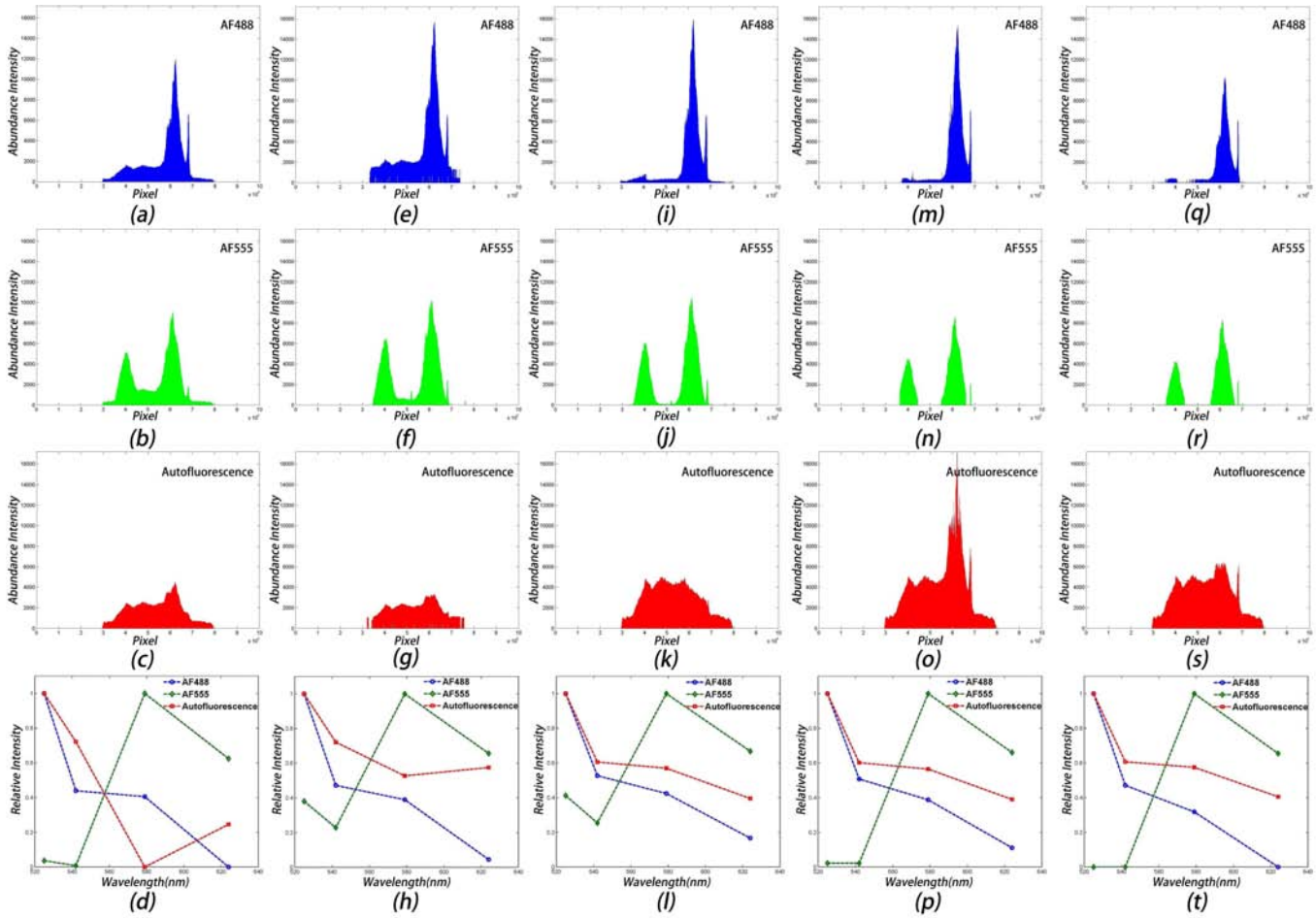


Fig. 9. Abundances (expressed as 1-D vectors) \mathbf{C} of AF488, AF555, AF, and their spectra \mathbf{S} from top row to bottom row for experiment II. The unmixed results obtained with (a)–(d) NMU, (e)–(h) L_0 -NMF, (i)–(l) L_1 -HALS, (m)–(p) S-NMF, and (q)–(t) TBCR-NMF.

The unmixed abundances \mathbf{C} (expressed as 1-D vectors) and endmember spectra \mathbf{S} are illustrated in Fig. 9(a)–(d) for NMU, Fig. 9(e)–(h) for L_0 -NMF, Fig. 9(i)–(l) for L_1 -HALS, Fig. 9(m)–(p) for S-NMF and Fig. 9(q)–(t) for TBCR-NMF, respectively. The TBCR-NMF achieves the most accurate unmixed results compared with other algorithms. Particularly, the first row in Fig. 9 displays that AF488 abundance intensities obtained with other algorithms still contain AF parts that are not fully removed. The second row in Fig. 9 shows that the AF parts have made contributions to the AF555 abundances with the NMU, L_0 -NMF and L_1 -HALS algorithms except the TBCR-NMF and S-NMF. The S-NMF has abnormal (too large) values for the AF abundance in Fig. 9(o), while TBCR-NMF can get slowly varying abundances of AF in Fig. 9(s). In general, the unmixed abundances of AF488 and AF555 from the TBCR-NMF algorithm [Fig. 9(q) and (r)] are more sparse than other algorithms. Moreover, the spectra obtained with NMU in Fig. 9(d), L_0 -NMF in Fig. 9(h), and L_1 -HALS in Fig. 9(l) are clearly different from the calibrated spectra in Fig. 6(b). However, the spectra obtained with S-NMF in Fig. 9(p) and TBCR-NMF in Fig. 9(t) are more accurate than other algorithms.

The SAD and the average $\overline{\text{SAD}}$ values of three unmixed endmembers for *in vivo* experiment II are shown in Table I.

We can see that the TBCR-NMF gets the smallest $\overline{\text{SAD}}$ (0.0961) and the best unmixing performance.

D. In Vivo Experiments III and IV

In this section, using another two *in vivo* BALB/c mouse experiments, we further compare the proposed method with three recently published unmixing methods which also utilize the spatial information in the multispectral images. Specifically, besides the S-NMF that has good unmixing performance, we also use the following methods for performance comparison: the beta compositional model based spatial-spectral (BCM-spatial) algorithm³ [18], sparse unmixing via variable splitting augmented Lagrangian and total variation (SparseTV) algorithm⁴ [19], and regularized simultaneous forward-backward greedy (RSFoBa) algorithm⁵ [20]. The BCM-spatial method assumes beta-distributed endmembers and identifies pixels with similar proportion values to the pixel under unmixing by identifying the K-nearest spatial-spectral neighbors. The SparseTV algorithm

³ <http://engineers.missouri.edu/zarea/2014/11/code-beta-compositional-model-unmixing/>

⁴ <http://www.lx.it.pt/~bioucas/publications.html>

⁵ <http://levir.buaa.edu.cn/publications.html>

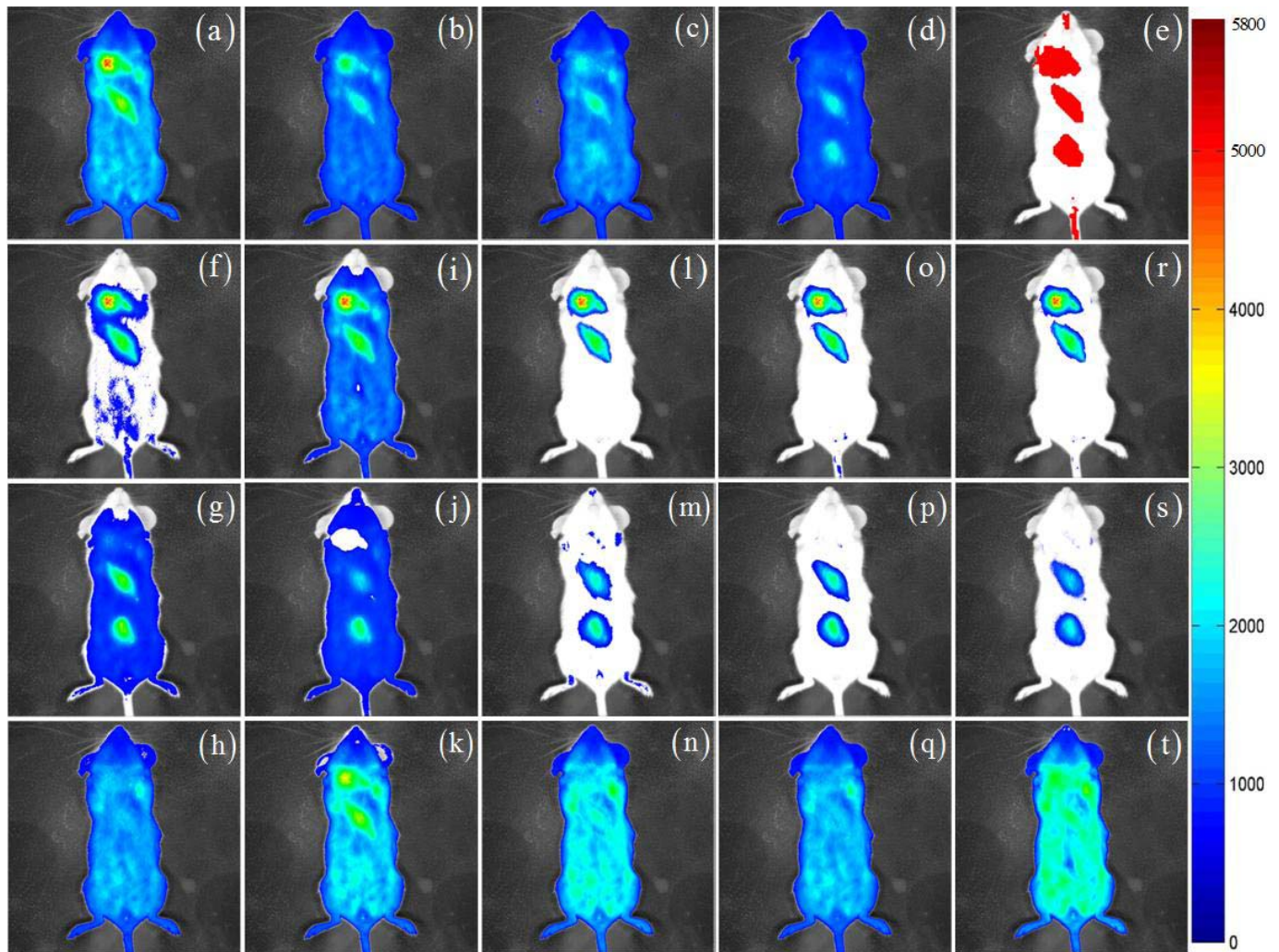


Fig. 10. (a)–(d) Raw fluorescence (AF488 and AF555) images for experiment III acquired at the 525, 542, 579, and 624 nm emission filters respectively, the first two images are excited at 474 nm and the last two images at 500 nm. (e) Classification results. The different unmixed results obtained with (f)–(h) BCM-spatial, (i)–(k) SparseTV, (l)–(n) RSFoBa, (o)–(q) S-NMF, and (r)–(t) TBCR-NMF.

includes the total variation regularization to the classical sparse regression formulation to exploit the spatial-contextual information present in the multispectral images. The RSFoBa algorithm solves a regularized least squares problem in sparse semisupervised unmixing by enforcing a spatial-contextual coherence within the multispectral images. All algorithms assume that the number of endmembers is 3. Except for the BCM-spatial method without *a priori* knowledge, the SparseTV and RSFoBa methods exploit *a priori* knowledge from the large number of spectral signatures in the United States Geological Survey spectral library, in which there are some similar spectral signatures simulating the endmember signatures for fluorescence dyes. All the parameters used in these algorithms are default values recommended in [18]–[20].

In the last two experiments, the AF488 and AF555 used as two target fluorophores are diluted to $0.1 \mu\text{gml}^{-1}$. The raw fluorescence images that are sparsely acquired at the 525, 542, 579, 624 nm emission filters for the experiment III are displayed in Fig. 10(a)–(d), which show that AF488 (50 ng) is subcutaneously injected at the upper and middle parts of

mouse's body and AF555 (50 ng) at the middle and bottom parts of the body. The AF488 is excited at 474 nm and displayed nearly on all four channels while the AF555 is excited at 500 nm and emitted on the 579 nm and 624 nm channels. Using linear scaling for the pseudo-color mapping can clearly demonstrate detailed changes in the strong AF, which has clear spectral overlap with the spectra of AF488 and AF555 in all spectral channels. In addition, there are also distinct cross-talks between these two target fluorophores. This strong spectral overlapping is also displayed clearly at the calibrated spectra of AF488, AF555, and AF in Fig. 6(c).

Fig. 10(e) shows that the red target regions of the two fluorophores are successfully separated from the AF region, though there are two very small red target regions remained in the background regions of mouse's head and tail. This small noisy misclassification does not change the global target/background segmentation and has not sacrificed the unmixing performance of TBCR-NMF [Fig. 10(r)–(t)], which is still the best among all methods (see Fig. 10). It is worth noting that the global target/background segmentation offered

TABLE II
SAD AND $\overline{\text{SAD}}$ RESULTS ON THE *In Vivo* EXPERIMENTS III AND IV (THE SMALLER VALUES MEAN BETTER RESULTS. THE NUMBERS IN BOLD REPRESENT THE BEST PERFORMANCE)

| Methods | p priori knowledge | Experiment III | | | | Experiment IV | | | |
|-------------|--------------------|----------------|--------|--------|-------------------------|---------------|--------|--------|-------------------------|
| | | AF488 | AF555 | AF | $\overline{\text{SAD}}$ | AF488 | AF555 | AF | $\overline{\text{SAD}}$ |
| BCM-spatial | no | 0.0795 | 0.0261 | 0.1610 | 0.0889 | 0.0714 | 0.1102 | 0.1006 | 0.0941 |
| SparseTV | yes | 0.1087 | 0.2987 | 0.0068 | 0.1381 | 0.0472 | 0.1532 | 0.0287 | 0.0789 |
| RSFoBa | yes | 0.0306 | 0.1794 | 0.0138 | 0.0746 | 0.0867 | 0.1584 | 0.0148 | 0.0866 |
| S-NMF | yes | 0.0240 | 0.1785 | 0.0134 | 0.0720 | 0.0718 | 0.1985 | 0.0132 | 0.0945 |
| TBCR-NMF | no | 0.0216 | 0.1684 | 0.0148 | 0.0683 | 0.0303 | 0.1886 | 0.0145 | 0.0778 |

TABLE III
TOTAL COMPUTATION RUN TIMES (INCLUDING PREPROCESSING TIMES) IN SECONDS FOR THE FIVE SUM METHODS [INTEL CORE i5-4460 QUAD-CORE 3.2 GHz CPU, RAM 8.0 GB]

| Cases | BCM-spatial | SparseTV | RSFoBa | S-NMF | TBCR-NMF |
|-------|---------------|---------------|---------------|---------------|---------------|
| 1 | 201.38 (2.84) | 140.90 (2.77) | 491.01 (2.92) | 298.41 (2.75) | 627.99 (2.80) |
| 2 | 197.91 (2.46) | 142.00 (2.30) | 484.13 (2.40) | 297.62 (2.28) | 590.03 (2.40) |

by TBCR-NMF is sufficiently effective to not only facilitate extracting the general endmember information for NMF initialization but also improve the NMF decomposition by imposing the sparseness constraint solely on the target regions. From the visual valuation, the second- and third-best unmixing performances are achieved by the S-NMF [Fig. 10(o)–(q)] and RSFoBa [Fig. 10(l)–(n)] methods, respectively. The BCM-spatial [Fig. 10(f)–(h)] method cannot fully remove the AF from the separated results of AF488 and AF555 components, while the SparseTV [Fig. 10(i)–(k)] method achieves the worst performance by making the two target fluorophores and AF mixed. Due to space limitations, we only show the unmixed results of experiment III in this paper. However, the overall performance of these methods in the experiments III and IV is listed in Table II, where the SAD and the average $\overline{\text{SAD}}$ values of three endmembers demonstrate that the proposed method achieves the smallest $\overline{\text{SAD}}$ (0.0683 for experiment III and 0.0778 for experiment IV) and the best unmixing performance.

The total run times (including the preprocessing times for mask extraction and/or improved Ncut) of the proposed TBCR-NMF method and other compared methods are tabulated in Table III. All the programs are executed in the MATLAB R2014b environment of an Intel Core i5-4460 Quad-Core 3.2 GHz CPU and 8 GB RAM. As can be observed, the SparseTV, BCM-spatial, and S-NMF methods require less computational time than the RSFoBa and TBCR-NMF methods. In addition, the computation times of the RSFoBa are approximately 80% of those of the TBCR-NMF, within which the HALS iterative algorithm incurs much computational cost compared with the simple multiplicative updating algorithm adopted within S-NMF. The run times of improved recursive Ncut and ATGP are only several seconds that make up only a very small proportion of total run times. Therefore, our future work is to reduce

computational cost of the HALS-based NMF in TBCR-NMF framework by optimizing the code and/or adopting smart update for fast HALS-based NMF. Further details about the fast HALS solutions and their computational complexity can be found in the recent works [9], [28], [37].

IV. CONCLUSION AND DISCUSSION

After exploiting the spatial distribution difference between multiple target fluorophores and background AF in fluorescence imaging measurements, we initialize and regularize the proposed TBCR-NMF algorithm with spatial information of target/background classification to get optimal fluorescence unmixing results (the source code of TBCR-NMF algorithm is available at <http://www.escience.cn/people/bjqin/research.html>). Specifically, we first propose the improved Ncut method to classify the fluorescence images into two kinds of groups: target fluorescence and background AF groups. We then extract the endmember spectra of multiple target fluorophores and AF from the classified target/background groups for accurately initializing the NMF. We have further regularized the HALS-based NMF decomposition with partial sparseness constraint being imposed on the abundances of target fluorophores but not the background AF. Experiments with synthetic and real fluorescence data show the proposed TBCR-NMF algorithm can blindly achieve the best unmixing performance compared with other NMF-based SUM methods and other state-of-the-art SUM methods that also utilize the spatial information in multispectral images.

ACKNOWLEDGMENT

The authors would like to thank the anonymous reviewers who contributed to considerably improve the quality of this paper. The authors would also like to thank G. Zhe for his evaluation work, Dr. Z. Yong-gang for inspiring discussion,

T. Tian-heng, and T. Li-ming for contributing to the project, and Dr. P. Jin-liang for supporting the experiments in fluorescence imaging. The authors declare that they have no competing interests.

REFERENCES

- [1] F. Leblond, S. C. Davis, P. A. Valdés, and B. W. Pogue, "Pre-clinical whole-body fluorescence imaging: Review of instruments, methods and applications," *J. Photochem. Photobiol. B, Biol.*, vol. 98, pp. 77–94, Jan. 2010.
- [2] F. L. Peña, J. L. Crespo, and R. J. Duro, "Unmixing low-ratio endmembers in hyperspectral images through Gaussian synapse ANNs," *IEEE Trans. Instrum. Meas.*, vol. 59, no. 7, pp. 1834–1840, Jul. 2010.
- [3] J. Plaza, E. M. T. Hendrix, I. García, G. Martín, and A. Plaza, "On end-member identification in hyperspectral images without pure pixels: A comparison of algorithms," *J. Math. Imag. Vis.*, vol. 42, pp. 163–175, Feb. 2012.
- [4] A.-S. Montcuquet, L. Hervé, F. Navarro, J.-M. Dinten, and J. I. Mars, "In vivo fluorescence spectra unmixing and autofluorescence removal by sparse nonnegative matrix factorization," *IEEE Trans. Biomed. Eng.*, vol. 58, no. 9, pp. 2554–2565, Sep. 2011.
- [5] R. Zdunek, "Regularized nonnegative matrix factorization: Geometrical interpretation and application to spectral unmixing," *Int. J. Appl. Math. Comput. Sci.*, vol. 24, no. 2, pp. 233–247, 2014.
- [6] J. Galeano, S. Perez, Y. Montoya, D. Botina, and J. Garzón, "Blind source separation of ex-vivo aorta tissue multispectral images," *Biomed. Opt. Exp.*, vol. 6, no. 5, pp. 1589–1598, 2015.
- [7] J. Xu *et al.*, "Sparse non-negative matrix factorization (SNMF) based color unmixing for breast histopathological image analysis," *Comput. Med. Imag. Graph.*, vol. 46, pp. 20–29, Dec. 2015.
- [8] B. Gao, H. Zhang, W. L. Woo, G. Y. Tian, L. Bai, and A. Yin, "Smooth nonnegative matrix factorization for defect detection using microwave nondestructive testing and evaluation," *IEEE Trans. Instrum. Meas.*, vol. 63, no. 4, pp. 923–934, Apr. 2014.
- [9] A. Cichocki, R. Zdunek, A. H. Phan, and S.-I. Amari, *Nonnegative Matrix and Tensor Factorizations: Applications to Exploratory Multi-Way Data Analysis and Blind Source Separation*. New York, NY, USA: Wiley, 2009.
- [10] P. O. Hoyer, "Non-negative matrix factorization with sparseness constraints," *J. Mach. Learn. Res.*, vol. 5, pp. 1457–1469, Dec. 2004.
- [11] Z. Yang, G. Zhou, X. Xie, S. Ding, J.-M. Yang, and J. Zhang, "Blind spectral unmixing based on sparse nonnegative matrix factorization," *IEEE Trans. Image Process.*, vol. 20, no. 4, pp. 1112–1125, Apr. 2011.
- [12] R. Rajabi and H. Ghassemian, "Sparsity constrained graph regularized NMF for spectral unmixing of hyperspectral data," *J. Indian Soc. Remote Sens.*, vol. 43, no. 2, pp. 269–278, 2015.
- [13] L. Tong, J. Zhou, X. Bai, and Y. Gao, "Dual graph regularized NMF for hyperspectral unmixing," in *Proc. Digit. Image Comput., Techn. Appl. (DICTA)*, Wollongong, NSW, Australia, 2014, pp. 1–8.
- [14] H. Liu and S. Li, "Target detection using sparse representation with element and construction combination feature," *IEEE Trans. Instrum. Meas.*, vol. 64, no. 2, pp. 290–298, Feb. 2015.
- [15] S. Yu, Y. Zhang, W. Liu, N. Zhao, X. Xiao, and G. Yin, "A novel initialization method for nonnegative matrix factorization and its application in component recognition with three-dimensional fluorescence spectra," *Spectrochim. Acta A, Molecular Biomolecular Spectrosc.*, vol. 86, pp. 315–319, Feb. 2012.
- [16] X. Tang, T. Xu, X. Feng, and G. Yang, "Uncovering community structures with initialized Bayesian nonnegative matrix factorization," *PLoS ONE*, vol. 9, no. 9, p. e107884, 2014.
- [17] C. Shi and L. Wang, "Incorporating spatial information in spectral unmixing: A review," *Remote Sens. Environ.*, vol. 149, pp. 70–87, Jun. 2014.
- [18] X. Du, A. Zare, P. Gader, and D. Dranishnikov, "Spatial and spectral unmixing using the beta compositional model," *IEEE J. Sel. Topics Appl. Earth Observ. Remote Sens.*, vol. 7, no. 6, pp. 1994–2003, Jun. 2014.
- [19] M.-D. Iordache, J. M. Bioucas-Dias, and A. Plaza, "Total variation spatial regularization for sparse hyperspectral unmixing," *IEEE Trans. Geosci. Remote Sens.*, vol. 50, no. 11, pp. 4484–4502, Nov. 2012.
- [20] W. Tang, Z. Shi, and Y. Wu, "Regularized simultaneous forward-backward greedy algorithm for sparse unmixing of hyperspectral data," *IEEE Trans. Geosci. Remote Sens.*, vol. 52, no. 9, pp. 5271–5288, Sep. 2014.
- [21] L. Fang, S. Li, X. Kang, and J. A. Benediktsson, "Spectral-spatial hyper-spectral image classification via multiscale adaptive sparse representation," *IEEE Trans. Geosci. Remote Sens.*, vol. 52, no. 12, pp. 7738–7749, Dec. 2014.
- [22] M. J. Canty, *Image Analysis, Classification and Change Detection in Remote Sensing*, 3rd ed. Boca Raton, FL, USA: CRC Press, 2014.
- [23] J. Shi and J. Malik, "Normalized cuts and image segmentation," *IEEE Trans. Pattern Anal. Mach. Intell.*, vol. 22, no. 8, pp. 888–905, Aug. 2000.
- [24] Z. Xu, H. Zhang, Y. Wang, X. Chang, and Y. Liang, " $L_{1/2}$ regularization," *Sci. China Inf. Sci.*, vol. 53, no. 6, pp. 1159–1169, 2010.
- [25] J. Sigurdsson, M. O. Ulfarsson, and J. R. Sveinsson, "Hyperspectral unmixing with l_q regularization," *IEEE Trans. Geosci. Remote Sens.*, vol. 52, no. 11, pp. 6793–6806, Nov. 2014.
- [26] A. Cichocki, R. Zdunek, and S.-I. Amari, "Hierarchical ALS algorithms for nonnegative matrix and 3D tensor factorization," in *Lecture Notes in Computer Science*, vol. 4666. London, U.K.: Springer, 2007, pp. 169–176.
- [27] W. Chen and M. Guillaume, "HALS-based NMF with flexible constraints for hyperspectral unmixing," *EURASIP J. Adv. Signal Process.*, vol. 2012, no. 54, pp. 1–14, 2012.
- [28] N. Gillis and F. Glineur, "Accelerated multiplicative updates and hierarchical ALS algorithms for nonnegative matrix factorization," *Neural Comput.*, vol. 24, no. 4, pp. 1085–1105, 2012.
- [29] Q. Du, N. Raksuntorn, N. H. Younan, and R. L. King, "End-member extraction for hyperspectral image analysis," *Appl. Opt.*, vol. 47, no. 28, pp. F77–F84, 2008.
- [30] Y.-X. Wang and Y.-J. Zhang, "Nonnegative matrix factorization: A comprehensive review," *IEEE Trans. Knowl. Data Eng.*, vol. 25, no. 6, pp. 1336–1353, Jun. 2013.
- [31] N. Gillis, "Nonnegative matrix factorization: Complexity, algorithms and applications," Ph.D. dissertation, Dept. Math. Eng., Univ. Catholique Louvain, Louvain-la-Neuve, Belgium, 2011.
- [32] F. van der Meer, "The effectiveness of spectral similarity measures for the analysis of hyperspectral imagery," *Int. J. Appl. Earth Observ. Geoinf.*, vol. 8, no. 1, pp. 3–17, 2006.
- [33] A. Plaza, P. Martínez, R. Pérez, and J. Plaza, "A quantitative and comparative analysis of endmember extraction algorithms from hyperspectral data," *IEEE Trans. Geosci. Remote Sens.*, vol. 42, no. 3, pp. 650–663, Mar. 2004.
- [34] N. Gillis and F. Glineur, "Using underapproximations for sparse nonnegative matrix factorization," *Pattern Recognit.*, vol. 43, no. 4, pp. 1676–1687, 2010.
- [35] R. Peharz and F. Pernkopf, "Sparse nonnegative matrix factorization with l^0 -constraints," *Neurocomputing*, vol. 80, pp. 38–46, Mar. 2012.
- [36] N. Otsu, "A threshold selection method from gray-level histograms," *IEEE Trans. Syst., Man, Cybern.*, vol. 9, no. 1, pp. 62–66, Jan. 1979.
- [37] G. Zhou, A. Cichocki, Q. Zhao, and S. Xie, "Nonnegative matrix and tensor factorizations: An algorithmic perspective," *IEEE Signal Process. Mag.*, vol. 31, no. 3, pp. 54–65, May 2014.



Binjie Qin (M'07) is currently an Associate Professor of Biomedical Engineering with Shanghai Jiao Tong University, Shanghai, China. Over the past years, his research has been focused on image registration for image guided therapy, system development for multispectral fluorescence imaging, and image denoising for X-ray fluorescence spectral images. His group has developed image guided surgery system and small animal optical imaging system that are successfully used in clinical applications. His current research interests include biomedical imaging, biomedical image processing, biomedical signal processing, and computer vision.



Chen Hu received the B.S. degree in biomedical Engineering from Xi'an Jiaotong University, Xi'an, China, in 2011, and the M.S. degree from Shanghai Jiao Tong University, Shanghai, China, in 2014.



Shaosen Huang received the B.S. degree and the M.S. degree in biomedical engineering from Shanghai Jiao Tong University, Shanghai, China, in 2011 and 2013, respectively.